nature portfolio

https://doi.org/10.1038/s41567-022-01512-3

Supplementary information

Nonlocal nonlinear phononics

In the format provided by the authors and unedited

Supplementary information for
Nonlocal nonlinear phononics

M. Henstridge[1], M. Först[1], E. Rowe[1], M. Fechner[1], A. Cavalleri[1,2]

[1] *Max Planck Institute for the Structure and Dynamics of Matter, 22761 Hamburg, Germany*

[2] *Department of Physics, Clarendon Laboratory, University of Oxford, Oxford OX1 3PU, United Kingdom*

S.1) Summary of the FSRS process

FSRS requires two incident electric fields, E_r and E_w, with respective carrier frequencies ω_r and ω_w chosen in the visible spectral range for this experiment. E_r has a narrow spectral bandwidth (< 1 THz) corresponding to a pulse duration of typically 1-3 ps. E_w is typically a coherent white light continuum pulse with a spectral bandwidth spanning tens of THz and temporal FWHM $\lesssim$ 100 fs. When the two pulses impinge on the $LiNbO_3$ crystal, a force $F = R^*(E_r + E_w)^2$ is then imparted onto a given mode Q that has Raman activity. For the FSRS process, we are concerned with the force component proportional to $E_r E_w$ which oscillates at the difference frequency $\omega_r - \omega_w$. The relevant equation of motion for the mode Q with eigenfrequency ω_Q and damping rate γ_Q is then

$$\ddot{Q} + 2\gamma_Q \dot{Q} + \omega_Q^2 Q = R^* E_r E_w \propto \cos[(\omega_r - \omega_w)t]. \quad \text{(S1)}$$

Any mode with frequency ω_Q can be stimulated through Eqn. (S1) as long as the white light continuum contains spectral weight at $\omega_r \pm \omega_Q$. The stimulated mode Q then mixes with E_r via the Raman tensor, generating a nonlinear polarization $P_{rQ} = \epsilon_o R^* E_r Q$ which oscillates at frequencies $\omega_r \pm \omega_Q$. The resulting scattered field E_{sc} is given by the inhomogeneous wave equation

$$\nabla^2 E_{sc} - \frac{n^2}{c^2}\frac{\partial^2 E_{sc}}{\partial t^2} = \frac{1}{\epsilon_o c^2}\frac{\partial^2 P_{rQ}}{\partial t^2} = \frac{1}{c^2}\frac{\partial^2 (R^* E_r Q)}{\partial t^2}. \qquad \text{(S2)}$$

Here, *n* is the index of refraction, *c* is the vacuum speed of light, and ϵ_o is the vacuum permittivity. Equations (S1) - (S2) describe a four-wave mixing process in which E_{sc} is ultimately emitted in the same direction as E_w [1]. When sent to a spectrometer, the two fields interfere in the frequency domain, with the resulting intensity given by

$$I_{FSRS}(\omega) = \left| \int (E_w + E_{sc}) e^{i\omega t} dt \right|^2. \qquad \text{(S3)}$$

As shown in Figure 2 of the manuscript, the frequency components of E_{sc} at $\omega_r - \omega_Q$ and $\omega_r + \omega_Q$ interfere with the incident field E_w constructively and destructively, respectively. All FSRS spectra shown in the manuscript are normalized to the power spectrum of E_w according to:

$$FSRS(\omega) = \frac{\left| \int (E_w + E_{sc}) e^{i\omega t} dt \right|^2}{\left| \int E_w e^{i\omega t} dt \right|^2}. \qquad \text{(S4)}$$

In the limit of a static Raman tensor, FSRS cannot discern whether a Raman tensor element is positive or negative, as in the case of an incoherent Raman scattering probe. The signals produced by both of these experiments is proportional to R^{*2}. However, contrary to the case of incoherent scattering, FSRS can detect a transient sign reversal of the Raman susceptibility. Particularly, because E_r is a long pulse and the phonon mode Q has a finite lifetime, FSRS probes the system response over a certain time window. If R^* experiences a sign change between the phonon excitation and the nonlinear mixing processes, the probe response contains a *heterodyne* signal in which the mode Q, launched at a time when R^* has reversed sign, mixes with the field E_r throughout later times when R^* recovers its original sign. This interference term produces a sign change in the final FSRS signal.

S.2) FDTD simulations of the FSRS signal for cases of a transiently negative Raman coefficient

To confirm that the pump-induced changes observed in the experiment result from the bulk, we used a finite-different time-domain (FDTD) routine to simulate the FSRS signal after propagation through a material of 50 μm thickness for three cases: a static Raman coefficient (Figure S1(a)), a Raman coefficient which reverses sign in the first 3 μm of the material (Figure S1(b)) and a Raman coefficient that reverses sign throughout the bulk of the material (Figure S1(c)). In the latter two cases, we assumed that the transient Raman tensor propagates at the velocity of the probe pulses. Upon comparison of panels S1(a) and (b), it is clear that changes to the FSRS spectrum are marginal if the Raman coefficient is only dynamic within a 3 μm depth. However, as seen in Figure S1(c), the FSRS signal reverses sign by 50% when the dynamically negative Raman coefficient propagates throughout the bulk.

S.3) Sample preparation

All measurements were performed at room temperature and in ambient air. The sample investigated was a 50μm x-cut $LiNbO_3$ single crystal which was coated on the back side with an anti-reflection layer designed for 400 nm wavelengths. This reduced the prominence of fringes in the white light continuum spectrum due to Fabry-Perot interferences.

S.4) Experimental Setup

a) Mid-IR pump.

A regeneratively amplified Ti:sapphire amplifier operating at a 1 kHz repetition rate was used for the experiments, delivering pulses of ~100 fs duration at 800 nm carrier wavelength. 4 mJ of the pulse energy was used to pump an optical parametric amplifier, which produced 1.2 mJ of combined signal and idler pulse energies when tuned to a signal wavelength of 1520 nm. The two near-infrared beams were then used to generate mid-infrared pulses of 12 μJ energy and 20 THz central frequency (7 THz FWHM) by difference frequency mixing in a GaSe crystal.

b) FSRS probe.

To construct the FSRS probe, a portion of the remaining 800 nm output from the regenerative amplifier was split into two paths. The first path employed roughly 1μJ in order to generate a white light continuum pulse in a CaF_2 substrate. Using a motorized stage, the substrate was kept under constant translational motion in order to avoid damage. The spectral weight of the continuum pulse extended to 350 nm wavelengths; however, the edge pass filter used to remove the residual 800 nm light reduced the shortest usable wavelength to 388 nm. The continuum pulse was collimated and then focused onto the sample using only reflective optics.

To generate the narrowband Raman pump field, 10 μJ pulses of the fundamental 800 nm was incident upon a 1.5 cm thick type-I BBO, generating 1.4 μJ of second harmonic with central wavelength of 400 nm (750 THz). The pulse envelope was characterized by cross correlation with the white light continuum pulse in a time-resolved two-photon absorption measurement in the 50 μm-thick $LiNbO_3$. The temporal width of the pulse envelope, which is shown in Figure S2, was

determined by the group velocity mismatch between the fundamental 800 nm pulse and the generated 400 nm pulse in the BBO [2]. The asymmetry in the intensity envelope results from the depletion of the 800 nm pulse as it passes through the crystal. The temporal width between the rising and falling edge of the pulse was roughly 3 ps.

c) FSRS data acquisition

In order to facilitate single-shot detection of the white light continuum pulses, the CCD of the spectrometer was triggered at the 1 kHz repetition rate of the regenerative amplifier. The narrowband Raman pump pulses were mechanically chopped at half the frequency (500 Hz), facilitating a consecutive narrowband pulse on/off sequence impinging upon the sample. To produce a given FSRS spectrum, we collected a series of shots (minimum 50,000) and binned the data such that the sum of the "on" shots was divided by the sum of the "off" shots. For all measurements, the delay between the white light continuum and narrowband pulses was fixed to 1.85 ps with respect to the time trace shown in Figure S1.

When performing time-resolved FSRS measurements, the mid-IR pump illuminated the sample during both "on" and "off" shots. The sum of the "on" shots was divided by the sum of the "off" shots, in the same manner as the equilibrium FSRS measurements. Thus, effects which are dependent on the carrier-envelope phase of the mid-IR pulse, which can vary over modulo 2π from shot to shot, are averaged out in both the "on" and "off" shots. This was essential for averaging out parasitic carrier-envelope phase dependent effects of the impinging mid-IR pulses on the white light continuum spectrum.

S.5) FSRS spectra under mid-IR excitation

a) Influence of temporal chirp in the white light continuum spectrum

In general, changes to the Raman response due to excitation with the mid-IR pump manifest on both the positive and negative frequency sides of the FSRS spectrum. However, there is a positive chirp of 2.5 fs/THz on the white light continuum pulse which causes higher frequencies to undergo dynamics at a slightly earlier time delay relative to the negative side. Figure S3 shows a plot of an unpumped FSRS spectrum along with data recorded at the maximum pump fluence of 185 mJ/cm^2 for two time delays. At τ = -0.08 ps, the peaks on the positive frequency side (highlighted in red) first exhibit a sign reversal due to the chirp on the probe. Then, at τ = -0.03 ps, the peaks on the negative frequency side (also highlighted in red) proceed to reverse sign.

b) Time-dependent FSRS spectra at the highest pump fluence

Figure S4 shows a temporal waterfall plot of FSRS spectra measured at the highest excitation fluence of 185 mJ/cm^2. From inspection, one can see that the peaks corresponding to both Q_{IR} and Q_P reverse sign shortly after zero time delay. Note that the peak corresponding to Q_P reverses sign at a slightly earlier time delay than that of Q_{IR}. This is a result of the temporal chirp on the continuum pulse discussed above in section S.5a.

The normalized peak amplitudes shown in Figures 5(d)-(e) of the main text were determined through fits to the spectra shown in Figure S4. Here, each spectrum was fit to a series of Lorentzian functions. The peak amplitudes for Q_{IR} and Q_P were extracted from these fits and then normalized to those of the equilibrium spectrum.

S.6) Detection of the soft mode polariton in the time-resolved white light transmission

Figure S5 shows time-resolved changes in the sample transmission of the white light continuum probe, induced by the mid-IR pulses. In this case, the long-pulse 400-nm field E_r is absent. Such measurements were routinely used to calibrate the timing of the pulses in the experiment. The transient signal consists of a cross correlation peak at time zero, which is followed by oscillations of the Q_P phonon-polariton. The Fourier transform of these oscillations (shown in the inset) reveals a broad spectrum with a central frequency of 3.6 THz and a bandwidth of 4 THz FWHM. This measurement agrees with the results of the FDTD simulations.

S.7) Consideration of the polariton and probe velocities

The velocity of the visible probe pulses relative to the excitations arising from the mid-IR pump was determined by considering the group refractive index of $LiNbO_3$ at 400 nm ($n_{g0} = 2.86$) [3] as well as the $\theta = 30°$ angle between the mid-IR pump and the white light continuum. In the rest frame of the polariton, the probe moves slower than it would in the case that it was collinear with the polariton; the effective group velocity is given by $v_g = c/n_g = c/(n_{g0}\cos(30°))$ where c is the speed of light in vacuum. Figure S6 shows the mapping of n_{g0} and n_g onto the dispersion relation for the c-axis modes, which was generated by using parameters from infrared reflectivity measurements in Reference 4. Notably, the group velocity line intersects the polariton branch of the 18.3 THz TO phonon at a frequency of 16 THz. This indicates that the probe is phase-matched to effects which result from the propagating 16 THz polariton.

The phase index in the 3 THz range is n_p = 5.15, yielding a ratio of v_g/v_p= 1.56. The corresponding velocity line was then used for the plot of Figure 4(b) of the main text and in the

calculations which account for the velocity mismatch between the probe and the propagating reduction of the Raman tensor (see Supplementary Section S.8).

S.8) Time-domain model of the FSRS process

Here, we discuss the model that was used to produce the calculations shown in Figures 4(a) and 5(d)-(e) of the main text. The fields for the FSRS probe were modelled as

$$E_w(t) = E_{wo} e^{-t^2/2{t_w}^2} \cos(\omega_w t) \quad \text{(S5)}$$

$$E_r(t) = E_{ro} e_r(\mathrm{t}) \cos(\omega_r t) \quad \text{(S6)}$$

$E_w(t)$ served as a model white light continuum field, with t_w= 3 fs to ensure a large spectral bandwidth. $E_r(t)$ modelled the narrrowband field used in the experiments, and $e_r(\mathrm{t})$ is an interpolation of the pulse envelope shown in Figure S2. Following the discussion presented in Section S3, the equation of motion for the n$^{\mathrm{th}}$ c-axis mode was modelled as

$$\ddot{Q_n}(t) + 2\gamma_n \dot{Q_n}(t) + \omega_n^2 Q_n(t) = R_n^* E_r(t) E_w(t). \quad \text{(S7)}$$

The polarization resulting from the mixing of Q_n with the narrowband field via the Raman tensor is

$$P_n(t) = R_n^* Q_n(t) E_r(t). \quad \text{(S8)}$$

The radiated field $E_n(t)$ is proportional to the time-derivative of the polarization

$$E_n(t) \propto \frac{\delta}{\delta t}[R_n^* Q_n(t) E_r(t)] \quad \text{(S9)}$$

The FSRS spectrum as a function of frequency f is then given by

$$FSRS(f) = \frac{\left|\int (E_w(t) + \sum_n E_n(t)) e^{i\omega t} dt\right|^2}{\left|\int E_w(t) e^{i\omega t} dt\right|^2}. \quad \text{(S10)}$$

To model the equilibrium FSRS spectrum, the parameters R_n^* and γ_n were chosen so that Eq. S10 fits the experimental data.

Our model for the dynamic FSRS spectra resulting from mid-IR excitation assumes that R_n^* becomes time-dependent and consists of two components:

$$R_n^*(t) = R_n^-(t) + R^{16}(t) \quad \text{(S11)}$$

Here, $R_n^-(t)$ corresponds to a transient reduction of the equilibrium Raman tensor for the nth c-axis mode, and $R^{16}(t)$ models the oscillatory component responsible for the second-order scattering. The shape of $R_n^-(t)$ was determined by first assuming that the ferroelectric polarization P is reduced over the same time scale as the data reported in Ref. 5. First principles calculations of the Raman tensors $R_{IR}^*(P)$ and $R_P^*(P)$ (see Figure 5(b) of the main text) were then mapped onto the time-dependent polarization in order to produce $R_{IR}^*(t)$ and $R_P^*(t)$. Our model then assumes that these Raman tensors propagate throughout a 50 μm sample volume with a group velocity equal to the soft mode polariton phase velocity. To account for the velocity mismatch between the propagating $R_n^*(t)$ and the FSRS probe, the velocity line of the probe was projected onto the space-time maps for the propagating Raman tensors, and an integral along the velocity line was carried out for each time step. This produces the effective $R_{IR}^-(t)$ and $R_P^-(t)$ which are seen in the rest frame of the probe. For each data set, the degree of polarization reduction was adjusted in order to produce a given $R_{IR}^-(t)$ and $R_P^-(t)$ which produced calculations that best fit the data. The Raman tensors of the two additional c-axis modes which appear in the Raman spectrum at 8.3 THz and 10 THz were assumed follow the same dynamics as $R_P^-(t)$.

$R^{16}(t)$ was assumed to have the form:

$$R^{16}(t) = A\left(\frac{Erf[at]}{2} + \frac{1}{2}\right)\exp[-\pi\gamma t]\cos[2\pi f t + \phi] \quad \text{(S12)}$$

where $Erf[at]$ is an error function with rise parameter a that was chosen by integrating the Gaussian envelope of the mid-IR pulse used in the experiments. Additionally, γ is the lifetime of the 18.3 THz mode extracted from infrared measurements reported in Ref. 4, f was taken to be 16 THz, A was chosen as a fit for each data set, and ϕ is the phase of the oscillation. Generally, the phase ϕ of a linearly driven polariton is dependent on the carrier envelope phase (CEP) of the excitation pulse. In the experiments, the CEP of the mid-IR source fluctuates randomly from shot to shot, hence the time-resolved FSRS measurements were averaged over ~ 100,000 shots. To account for the phase averaging, equations S1 – S5 were evaluated from $\phi = 0\ to\ 2\pi$ in steps of $\pi/2$ for each delay t_d between the FSRS probe and $R_n^*(t + t_d)$. The expression which describes the simulated CEP-averaged FSRS spectrum for a given t_d is then:

$$I_{FSRS}(f)_{t_d} = \frac{\sum_\phi \left| \int (E_w(t) + \sum_n E_n(t)) e^{i\omega t} dt \right|^2}{\sum_\phi |\int E_w(t) e^{i\omega t} dt|^2} . \quad \text{(S13)}$$

S.9) DFT calculations of the Raman tensor in the presence of ferroelectric polarizations

The dependence of the Raman tensor elements on the ferroelectric polarization in $LiNbO_3$ was mapped out by utilizing the first-principle framework of density functional theory (DFT) calculations. We performed our computations with the Vienna ab-initio simulation package VASP.6.2 [6]. Moreover, for the phonon calculation, we used the Phonopy software package [7]. Our computations further utilized pseudopotentials generated within the Projected Augmented Wave (PAW) [8] method. Specifically, we take the following configurated default potentials: Li $2s^1$, Nb $4p^6 5s^1 4d^4$, and O $2s^2 2p^4$. We applied the PBEsol [9] approximation for the exchange-correlation potential. As a numerical setting, we used a 9x9x9 Monkhorst [10] generated k-point-

mesh sampling of the Brillouin zone and a plane-wave energy cutoff of 750 eV. The self-consistent calculations were reiterated until the change in total energy becomes less than 10^{-9} eV. Last, to compute the Raman tensor elements, we followed the approach of Ref. 11 and determined the R* elements from the induced change in the permittivity due to phonon displacement.

The starting point of our investigation was the ferroelectric ground state of $LiNbO_3$. To create a force-free reference configuration, we first structurally relaxed the LNO unit-cell in DFT. We initialized the computation with the experimental structure with symmetry R3c of Ref. 12. We then minimized the system until the Hellman Feynman forces on the atoms and the pressure on the unit cell became less than 0.1 eV/Ang. Tab. S1 contains the final structure. For this atomic arrangement, we then computed the phonon spectrum at the zone center and identified the four polar A_1 modes at the frequencies noted in the lower part of Tab S1. All results agree with experimental findings.

Next, we constructed the reversed ferroelectric (FE) polarization configuration by inverting the positions of all atoms. Further, we built the centrosymmetric state, which lies in between the two FE states. Utilizing these three states, we finally computed the atomic displacement field, which connects all three states. In Figure S7, we show the evolution of the FE polarization, calculated by the Berry-Phase Approach[13,14] along this displacement field. Note that $\lambda=0$ corresponds to the centrosymmetric state.

Finally, we applied the approach of Ref. 11 to compute the Raman tensor for the structures along this trajectory. Note that we recalculated the phonon spectrum for each structural configuration to

obtain the corresponding correct eigendisplacements of the phonons. The right panel of Fig. S7 shows the resulting R* dependence. An apparent reduction and sign change become evident upon passing through the centrosymmetric state, with exception to the 10.1 THz mode, which remains finite through the transition. When restoring inversion symmetry, the phonon modes recapture their unique character to be either infrared or Raman active. In the centrosymmetric state, LNO exhibits three polar modes and one Raman active mode, which become the c-axis polar modes in the ferroelectric phase. The 10.1 THz mode corresponds to the original Raman mode, which maintains its Raman activity, and thus a nonzero R*, in the centrosymmetric state.

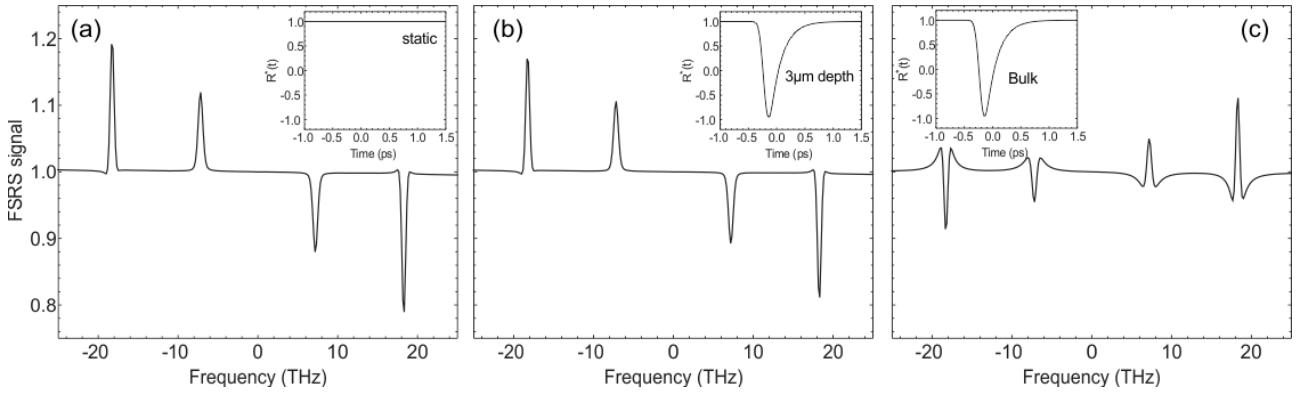

Figure S1. FDTD simulations of the FSRS probe after propagation through a material of 50 μm thickness for the cases of (a) a static Raman coefficient (b) a Raman coefficient that is transiently negative in the first 3 μm of the material depth (c) a transiently negative Raman coefficient which propagates throughout the bulk material. The insets shows the functional form of $R^*(t)$ assumed for the calculations.

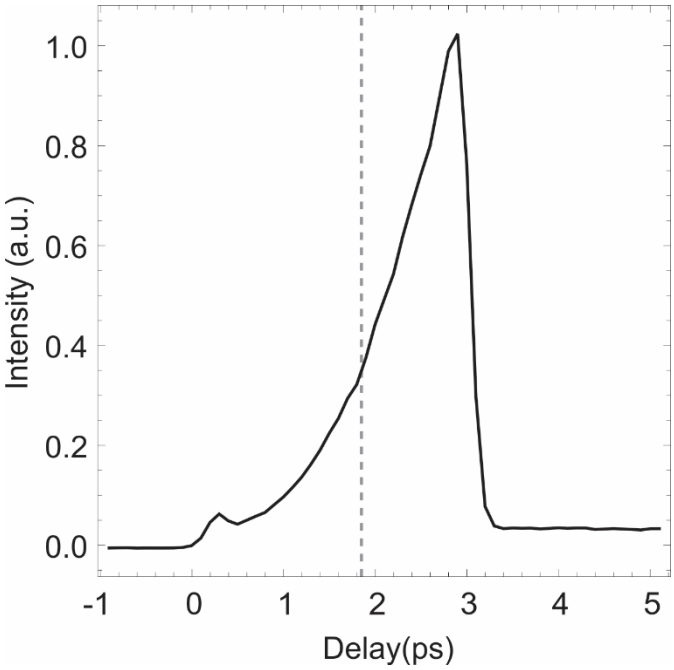

Figure S2. Intensity envelope of the narrowband field used in the FSRS probe, as obtained from two-photon absorption measurements in the 50 μm thick $LiNbO_3$ sample. The dashed line indicates the fixed position of the white light continuum pulse during the FSRS measurements.

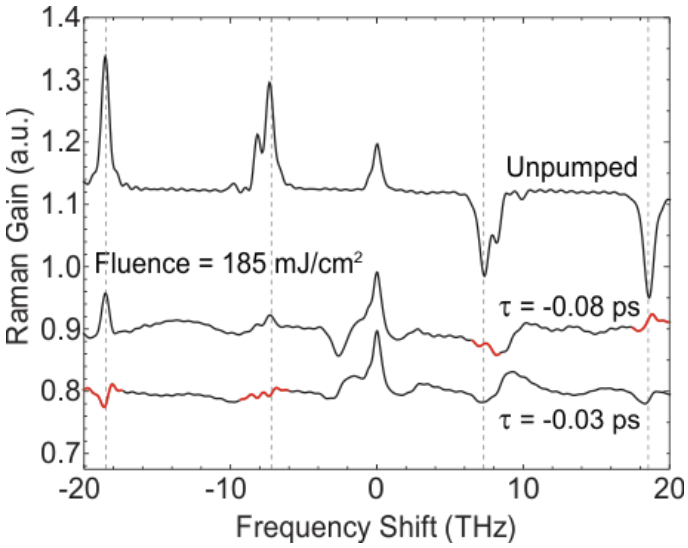

Figure S3. Response of the positive and negative frequency sides of the FSRS spectrum to changes induced by the mid-IR pump. As highlighted in red, the peaks on the positive side undergo dynamics at a slightly earlier time delay relative to the negative side. This is a result of the fact that the white light continuum pulse used in the FSRS probe has a positive chirp of 2.5 fs/THz.

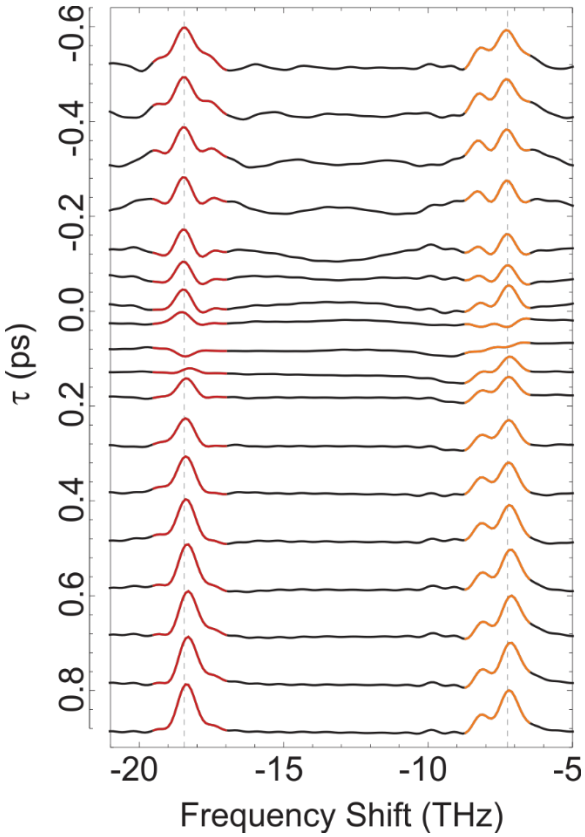

Figure S4. A temporal waterfall plot of the FSRS spectra recorded at the highest excitation fluence of 185 mJ/cm^2. Fits to these spectra were used to determine the normalized peak amplitudes shown in Figures 5(d)-(e) of the main text.

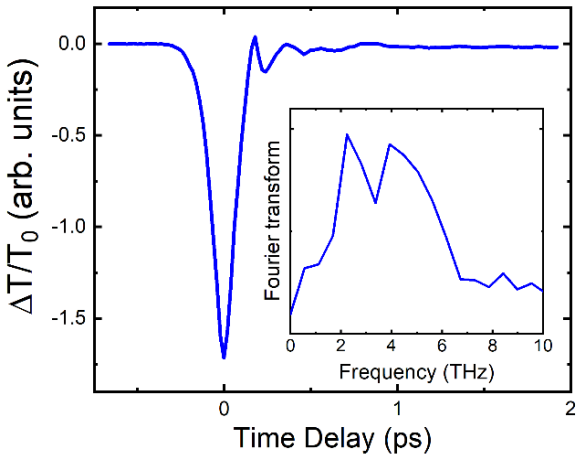

Figure S5. Time-resolved transmission of the white light continuum probe pulses as a function of time delay after mid-IR excitation. Note that the narrowband field E_r is absent in these measurements. The signal at time zero corresponds to a cross-correlation of the two pulses, and the following oscillatory component is attributed to the Q_P phonon-polariton. Shown in the inset is the Fourier spectrum of the oscillation, which agrees well with the spectrum of the Q_P phonon-polariton predicted by FDTD simulations.

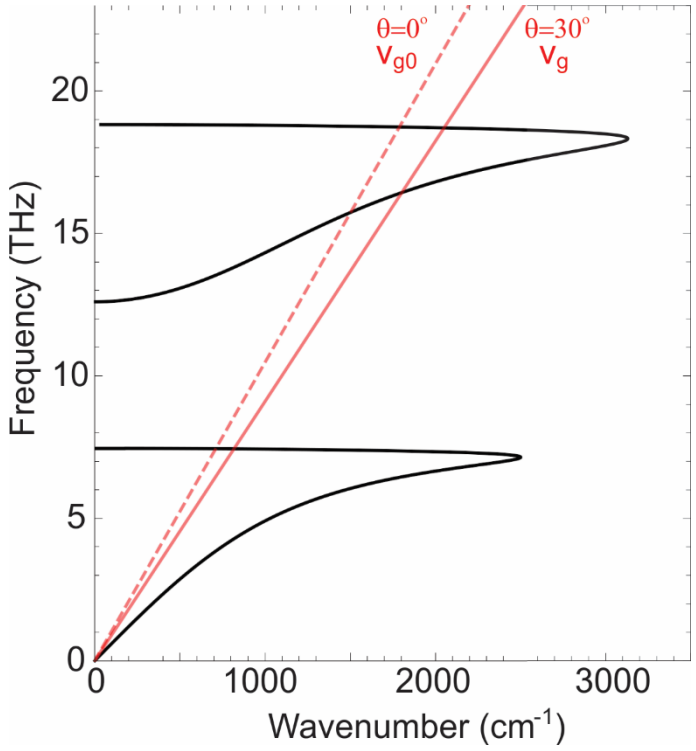

Figure S6. Black curve: Dispersion relation for the c-axis modes in $LiNbO_3$ plot using parameters obtained from Ref. 4. The slope of the dashed red curve indicates the group velocity of a pulse with carrier wavelength of 400 nm, and the solid red curve indicates the effective group velocity of such a pulse propagating at an angle of 30° relative to the polariton.

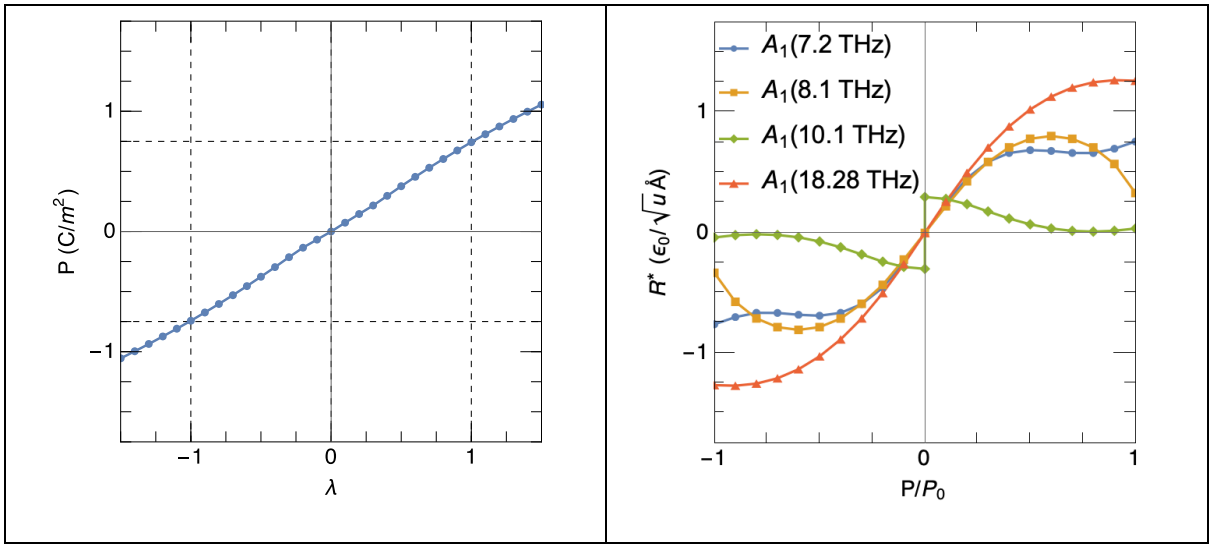

Figure S7. Left Panel: Total polarization as a function of structural distortion going from the $-P_0$ ferroelectric state to the inverted $+P_0$ state crossing the centrosymmetric state in the middle. Right panel: Raman tensor of the four polar A_1 modes in $LiNbO_3$

R3c	Theo.	Expt.[12]			*R-3C*			
a_{hex}	5.13 Å	5.15 Å			5.13 Å			
c_{hex}	13.81 Å	13.86 Å			13.81 Å			
Atomic positions:								
	Wykoff pos.	x	y	Z	Wykoff pos.	x	y	Z
Li	6a	0	0	0.78902	6a	0	0	0.25
Nb	6a	0	0	0.00674	6b	0	0	0
O	18b	0.04711	0.34397	0.07142	18e	0.61996	0	0.25
Phonons:								
phonon mode	Theory [THz]	Exp.[15] [THz]						
A1	7.20	7.55						
A1	8.10	8.24						
A1	10.06	9.95						
A1	18.28	18.95						

Table S1. Structural parameters in the hexagonal setting and phonon frequencies from DFT (this work) and experimental results

References

[1] Lee, S. Y., Zhang, D., McCamant, D. W., Kukura, P. & Mathies, R. A. *J. Chem. Phys.* **121**, 3632–3642 (2004).

[2] E. Pontecorvo, S.M. Kapetanaki, M. Badioli, D. Brida, M. Marangoni, G. Cerullo, and T. Scopigno *Opt. Express*, **19**, 1107–1112 (2011).

[3] Zelmon, D. E., Small, D. L. & Jundt, D., *J. Opt. Soc. Am. B* **14**, 3319 (1997).

[4] Barker, A. S. & Loudon, *Phys. Rev.* **158**, 433–445 (1967).

[5] Mankowsky, R., Von Hoegen, A., Först, M. & Cavalleri, *Phys. Rev. Lett.* **118**, 197601 (2017).

[6] G. Kresse and J. Furthmüller, *Phys. Rev. B* **54**, 11 169 (1996)

[7] Atsushi Togo and Isao Tanaka, *Scr. Mater.*, **108**, 1-5 (2015)

[8] G. Kresse and D. Joubert, *Phys. Rev. B* **59**, 1758 (1999)

[9] G. I. Csonka, et al., *Phys. Rev. B* **79**, 155107 (2009).

[10] Monkhorst, H. & Pack, *Phys. Rev. B* **13**, 5188 (1976).

[11] D. Porezag and M. R. Pederson, *Phys. Rev. B* **54**, 7830 (1996).

[12] S. C. Abrahams et al., J. Phys. *Chem. Solids* **27**, 997 (1966)

[13] R. D. King-Smith and D. Vanderbilt, *Phys. Rev. B* **47**, 1651 (1993).

[14] R. Resta, *Ferroelectrics* **136**, 51 (1992).

[15] A. Ridah, M. D. Fontana, and P. Bourson, Phys. Rev. B **56**, 5967 (1997).